Full Paper
Journal of Nano Materials Impact 2026, 02 (02) 38-46

Growth Highly Crystalline, Phase-Pure VO_2(M) Nanotube Through Two-Step Atomic Layer Deposition

Ahmed Al-Haddad
Department of Chemistry, College of Science, Mustansiriyah University, 10052 Baghdad, Iraq.

Abstract

Vanadium dioxide (VO_2) nanotube arrays were synthesized by combining the atomic layer deposition (ALD) through the anodic alumina templates (AAT) using vanadium oxytriisopropoxide (VTIP) and H_2O as precursors. A two-step deposition strategy was developed: an initial 60-cycle ALD seed-mediated layer was annealed at 520 °C for 2 h under a controlled Ar gas flow to crystallize the seed-mediated, followed by 340 additional ALD cycles at 400 °C to grow a crystalline VO_2 layer. The resulting nanotubes were characterized by SEM, XRD, TEM, and HRTEM. SEM confirmed highly ordered, uniform nanotube arrays with a 60 nm diameter and a 16.13 nm wall thickness. XRD of the one-step annealed sample revealed a nanocrystalline, mixed-valence V_xO_y material containing VO_2(M), residual V_2O_5, and probable Magnéli phases. In contrast, the two-step deposition produced phase-pure monoclinic VO_2(M) with sharp, high-intensity reflections and no detectable V_2O_5. HRTEM and FFT confirmed continuous lattice fringes and sharp diffraction spots indexed to the VO_2(M) phase, with a measured d-spacing of ~0.3214 nm. Raman spectroscopy confirmed the absence of the diagnostic V_2O_5 at ~994 cm^{-1} in the two-step sample, while this mode was clearly present in the one-step annealed sample, independently corroborating the phase purity of the two-step VO_2(M) nanotubes. The seed-mediated layer crystallized under Ar gas provided an ideal platform for highly crystalline growth, resulting in a continuous, well-ordered atomic lattice. This strategy of two-step ALD in a precise condition of each step enables the formation of high-quality VO_2 nanotube arrays (through AAT pores) with specific control over phase, morphology, and crystallinity, present promising prospects for applications in sensors, smart windows, and energy storage devices.

Keyword: vanadium dioxide • atomic layer deposition • monoclinic phase • nanotube • highly crystalline growth • anodic alumina templates.

Downloaded from https://nanomatimp.uomustansiriyah.edu.iq/

Introduction

Vanadium dioxide (VO_2) is a prototypical strongly correlated oxide that undergoes a reversible metal–insulator transition (MIT) near 68 °C, accompanied by a structural transformation from a low-temperature monoclinic (M1) insulating phase to a high-temperature tetragonal rutile metallic phase[1-3]. This first-order transition produces dramatic changes in electrical resistivity (by up to four to five orders of magnitude) and in infrared transmittance, making VO_2 a compelling material for applications in resistive switching, neuromorphic computing, smart thermochromic windows, and reconfigurable photonic devices[4-6]. The transition temperature, hysteresis width, and resistivity contrast are all exquisitely sensitive to the microstructure, stoichiometry, and strain. For this reason, more effort on VO_2 thin films has been driven for controlling crystallinity and improving the phase purity[5]. Among the many vanadium oxide polymorphs, monoclinic M1 is the most valuable technologically and yet the most elusive to stabilize selectively. It has a narrow thermodynamic window, and competing oxides such as V_2O_5 or the formation of Magnéli phases instead are highly probable[5, 7].

Electronic device performance closely tracks the crystalline quality[8-10]. In polycrystalline materials, grain boundaries, structural disorder, and interfacial defects broaden the hysteresis, suppress the resistivity switching ratio, and obstruct the transition[11, 12]. Crystalline VO_2 avoids such obstacles. The well-defined lattice delivers fewer defects and uniform strain; such materials switch more sharply, reach higher on/off ratios, and tighten the link between structure and function. They are usually grown by magnetron sputtering or pulsed laser deposition, most often on lattice-matched substrates such as TiO_2 (001) or c-Al_2O_3[13]. Both techniques, however, need high substrate temperatures, and neither coat three-dimensional or high-aspect-ratio architectures well. A low-temperature, conformal route to highly crystalline VO_2 therefore remains an open materials problem.

Atomic layer deposition (ALD) provides atomic-scale thickness control and excellent conformality on complex substrates[14, 15]. Because it relies on self-limiting surface reactions between alternating precursor pulses, ALD has become a standard method for high-quality oxide films, vanadium oxides included[16-18]. For VO_2, most processes pair a precursor such as tetrakis(ethylmethylamino)vanadium

***Address for correspondence:** Asst. Prof. Dr. Ahmed Al-Haddad, Department of Chemistry, College of Science, Mustansiriyah University, 10052 Baghdad, Iraq.
E-mail: ahmed.al-haddad@uomustansiriyah.edu.iq
ORCID: https://orcid.org/0000-0001-7296-4704

This is an open-access journal, and articles are distributed under the terms of the Creative Commons Attribution License (CC-BY) 4.0 License, which allows others to use, distribute, and reproduce in any medium for noncommercial purposes, as long as the original work is cited properly.

Info:
Submitted: 23 May 2026; **Revised:** 27 June 2026;
Accepted: 15 July 2026; **Published:** 15 Aug. 2026.
https://doi.org/10.71109/nmi.2026.2.2.41

Copyright © 2026. This work licensed under a Creative Commons Attribution Noncommercial 4.0 International License.

(TEMAV) with H_2O, O_3, or an O_2 plasma[16]. One limitation remains: as-deposited ALD vanadium oxide is almost always amorphous and must be annealed above roughly 400 °C to crystallize into the desired VO_2 phase[7]. That step is sensitive to oxygen partial pressure and often causes agglomeration, interfacial reactions, or unwanted vanadium oxide phases, particularly in ultrathin films[5]. Growing crystalline VO_2 directly by ALD, without an aggressive post-anneal, has therefore been difficult.

Several approaches have been tried to get around this. Annealing in a controlled atmosphere (oxygen-rich at 500 °C, for example, or hydrogen-containing at 350 °C) crystallizes amorphous ALD vanadium oxide into monoclinic VO_2, with a three-order-of-magnitude resistivity drop at the transition[19]. highly crystalline VO_2 has also been obtained on rutile (110) TiO_2 by post-reducing an ALD-grown vanadium oxide film, reporting that ALD can be combined with substrate templating to produce oriented crystalline films[19]. More recently, remote epitaxy has offered another route: a nanometer-thin amorphous Al_2O_3 interlayer grown by ALD between the substrate and the VO_2 film reduces interfacial clamping while maintaining crystalline registry, stabilizes the monoclinic M1 phase at room temperature, and increases the MIT amplitude without degrading crystallinity[13]. These advances show the promise of ALD for high-crystalline VO_2, yet a direct, in situ ALD process that yields phase-pure high-crystalline VO_2 has not been demonstrated.

Here, highly crystalline VO_2(M) nanotubes grown by ALD were reported. Using a metal-organic vanadium precursor with a controlled oxygen source. The nanotubes have a well-defined crystallographic orientation, sharp interfaces, and phase-pure monoclinic VO_2, as confirmed by X-ray diffraction (XRD), transmission electron microscopy (TEM), and Raman spectroscopy. These results establish ALD as a viable route to high-quality crystalline VO_2(M) for advanced electronic and photonic applications.

Experimental and Methods

Anodic alumina templates (AAT) were prepared by anodic oxidation of high-purity aluminum foil (99.995%) according to established procedures[20-23]. The template thickness (330 nm), pore order distance (110 nm), and pore diameter (60 nm) were controlled by the anodization time (8 min), electrolyte (0.3 M oxalic acid, 40 volt at 10 °C), and pore-widening time treatment (in 5 wt % H_3PO_4 at 30 °C for 14 min), respectively. Several samples of AAT with pore diameters of 60 nm and corresponding interpore distances of 50 nm were used. The AAT pore dimensions were fixed by choosing optimized anodization conditions[20, 24, 25].

The prepared AAT were placed inside the ALD chamber (Picosun SUNALETM R150 ALD), and the temperature was increased to 400 °C. A vanadium precursor (vanadium oxytriisopropoxide, VTIP) and H_2O were used as the V and O sources, respectively; N_2 was used as both carrier and purge gas (120 sccm). Typical pulse times for the vanadium precursor and H_2O were 0.1 s, and the N_2 purge time was 5 s. As traditional one-step deposition 400 cycles were applied to deposit V_xO_y nanotube sample. The samples were then annealed at 520 °C for 2 h under a controlled Ar gas flow. Thereafter, a new strategy was applied with two-step deposition by the initial 60 cycles to produce of ~2.4 nm continuous V_xO_y layer covering the entire AAT surface (including the pores surface). The samples were then annealed at 520 °C for 2 h under a controlled Ar gas atmosphere to crystallize the seed-mediated oriented layer (~2.4 nm) of VO_2. Subsequently, 340 additional cycles were deposited at 400 °C to grow a crystalline VO_2 layer on the seed-mediated oriented layer, giving a total of 400 cycles and a VO_2 wall thickness of ~16 nm. The cycle number can be adjusted according to the growth per cycle of the chosen VO_2 ALD chemistry to achieve the target wall thickness. In all samples, the wall thickness, diameter, and interpore distance of nanotubes were kept constant around ~16 nm, 60 nm, 50 nm, respectively. The nanotube length was controlled to 330 nm by choosing the same anodization time of AAT.

To open the pore bases and ensure uniform nanotubes, a poly[methyl methacrylate] (PMMA) layer was applied on the surface VO_2 layer over AAT to support the nanotubes after removing the remaining Al foil in 95 wt % of $CuCl_2$ + 5 wt % of HCl and the AAT in 5 wt % of H_3PO_4 at 30 °C for 60 min. The prepared samples of nanotube arrays were examined using Scanning Electron Microscope (SEM) from Hitachi S4800, high-resolution transmission electron microscopy (HRTEM) form FEI Titan 80-300, X-ray Diffraction (XRD) from Siemens D5000, and Raman spectrometer (Renishaw, UK) equipped with a laser 532 nm as excitation source and a grating configuration of 1200 gr/mm. The laser power at the sample was kept below 0.5 mW to avoid laser-induced heating or oxidation. Spectra were collected over the range of 100-1100 cm^{-1} with a spectral resolution of approximately 2 cm^{-1} and an accumulation time of 30 s.

Results and Discussion

Morphology of V_xO_y Nanotube Arrays

The morphology and structural evolution from the AAT to freestanding VO_2 nanotubes were examined by SEM. The images in **Figure 1** confirm that the combination ALD and AAT produces highly ordered and uniform V_xO_y nanotube arrays. **Figure 1a** shows a large-area top-view SEM image of the AAT. The entire field of view is covered by a highly uniform, hexagonally ordered nanopore array, indicating that the anodization process yielded a large-area template with few micrometers disordered range. The inset in (**Figure 1a**) presents a cross-sectional view of the template, revealing straight, parallel, and vertically aligned ~330 nm channels. This confirms that the AAT has a well-defined pore structure suitable for conformal ALD coating. **Figure 1b** provides a higher-magnification top view of the AAT. The pores are circular, monodisperse, and arranged in a close-packed hexagonal lattice. The pore diameter is controlled at approximately 60 nm with uniform interpore spacing. The high degree of order in the AAT is critical because it directly dictates the diameter, density, and spatial arrangement of the resulting VO_2 nanotubes.

Downloaded from https://nanomatimp.uomustansiriyah.edu.iq/

Copyright © 2026. This work licensed under a Creative Commons Attribution Noncommercial 4.0 International License.

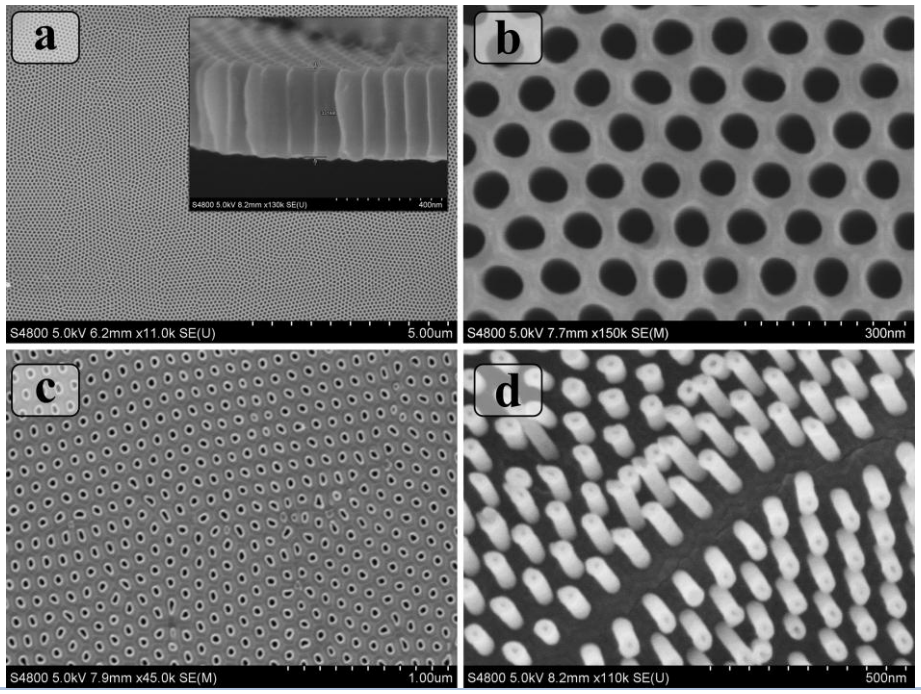


Figure 1. SEM images of (a) large area AAT (the inset is the cross-sectional of the AAT), (b) Highly ordered AAT pore arrays with controlled pore diameter of 60 nm, (c) VO_2 nanotubes after deposition and surface layer removing, and (d) freestanding VO_2 nanotubes attached to beneath PMMA layer.

After the ALD process and removal of the surface layer, the template still maintains its ordered pore structure, but the contrast changes because of the conformal V_xO_y coating inside the pores. **Figure 1c** shows the top view at this stage. The pores appear slightly darker and more defined, consistent with the formation of hollow V_xO_y nanotubes within the AAT pores. The surface layer removal exposes the nanotube openings while preserving the overall hexagonal ordering. This indicates that the ALD coating is uniform and continuous along the pore walls. **Figure 1d** shows a high-magnification SEM image of freestanding V_xO_y nanotubes supported by a PMMA layer. The nanotubes remain vertically aligned and retain the hexagonal arrangement transferred from the AAT. The nanotubes appear uniform, with smooth walls and open ends. The PMMA layer offers mechanical support during template removal, avoiding the nanotubes from bundling or collapsing[26, 27]. This confirms that the ALD of VO_2 through AAT pores strategy yields robust, freestanding V_xO_y nanotube with high-aspect-ratio array. The SEM analysis confirms that the ALD process successfully produces uniform nanotubes with controlled dimensions. The AAT governs the nanotube diameter, wall thickness, and spatial arrangement, while the PMMA support layer enables the fabrication of freestanding nanotube arrays.

Transmission electron microscopy (TEM) was employed to further evaluate the morphological characteristics and dimensional precision of the synthesized V_xO_y nanotubes. The TEM image in **Figure 2** clearly reveals a well-defined, hollow tubular structure, The inset of **Figure 2a** is the FFT pattern with diffuse halos, confirming crystalline nature of the as-deposited V_xO_y nanotube, this confirms the lack of long-range order in the as-deposited nanotube without the high-temperature annealing step.

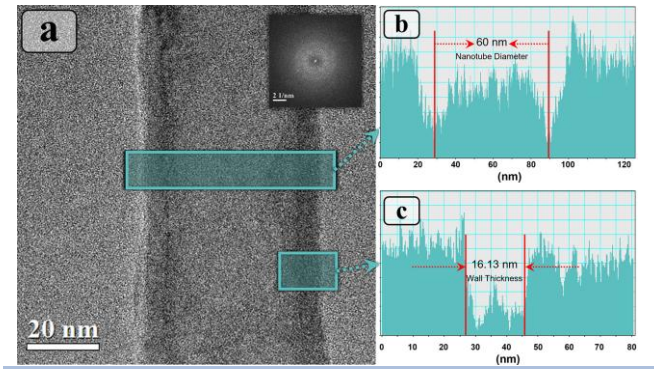


Figure 2. (a) TEM image and their line profiles of a single VO_2 nanotube diameter (b) and wall thickness (c).

The horizontal line profile across the nanotube (**Figure 2b**) shows a clear double-peak pattern, with the two maxima separated by 60 nm. That value matches the pore diameter of the original AAT, which suggests the ALD coating was conformal enough to preserve the template geometry. A second, local profile taken across the wall (**Figure 2c**) gives a uniform thickness of 16.13 nm that corresponds to a growth rate of about 0.04 nm/cycle.

Crystallinity of One-Step ALD Growth

The XRD pattern of the V_xO_y nanotube arrays after annealing at 400 °C for 2 h under a controlled Ar atmosphere in **Figure 3** shows broad but clearly resolved reflections in the 20–60° 2θ range. No sharp reflections corresponding to metallic Al or crystalline Al_2O_3 from the AAT are observed, indicating that the template was effectively removed. The strongest reflection appears at $2\theta \approx 26.42°$, with other prominent peaks at approximately 27.82°, 31.16°, 34.64°, 37.02°, 39.70°, 42.14°, 44.64°, 47.56°, 52.82°, and 55.28°.

Downloaded from https://nanomatimp.uomustansiriyah.edu.iq/

Copyright © 2026. This work licensed under a Creative Commons Attribution Noncommercial 4.0 International License.

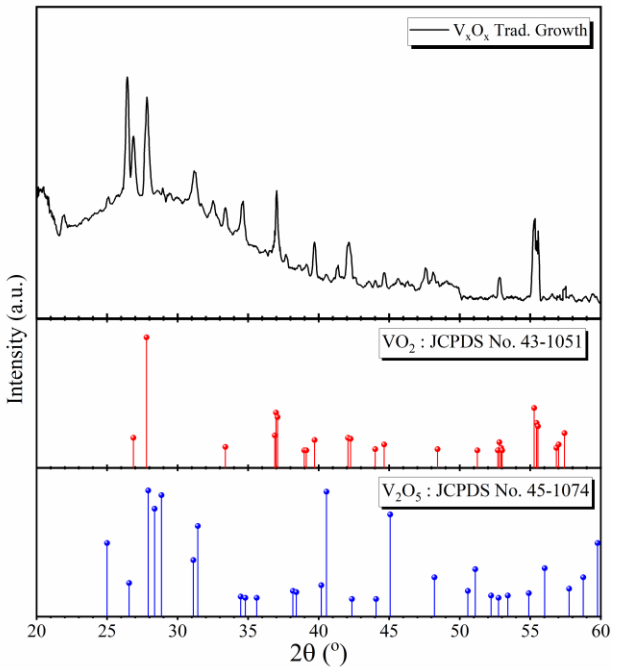


Figure 3. XRD Pattern of tradition (one-step) growth of V_xO_y nanotube annealed at 400 °C for 2 h under a controlled Ar gas flow.

The d-spacings were calculated using Bragg's law[28, 29]:

$$n\lambda = 2d \sin\theta \quad \text{... (1)}$$

with Cu Kα radiation, λ = 1.5406 Å. The crystallite size (D) was estimated using the Scherrer equation[28, 29]:

$$D = K\lambda/\beta \cos\theta \quad \text{... (2)}$$

where (K = 0.9) and (β) is the full width at half maximum in radians. The microstrain (ε) was estimated from[28, 29]:

$$\varepsilon = \beta/4 \tan\theta \quad \text{... (3)}$$

and the dislocation density (δ) was approximated as[28, 29]:

$$\delta = 1/D^2 \quad \text{... (4)}$$

The FWHM values were estimated directly from the XRD data; instrumental broadening was not subtracted. Therefore, the crystallite sizes reported here should be considered apparent values, and the true crystallite sizes may be slightly larger.

After the 400 °C anneal, the XRD data in **Table 1** show the V_xO_y nanotubes to be nanocrystalline and mixed-phase. The as-deposited layer (VTIP and H_2O at 400 °C) should be amorphous or poorly crystalline V_2O_5-like oxide, since VTIP supplies V and H_2O acts as the oxidant. Annealing at 400 °C delivers enough thermal energy for crystallization, but the vanadium is also somewhat reducing. Therefore, V^{5+} is partly reduced to V^{4+} or V^{3+}, leaving a mixed-valence V_xO_y material.

The reflections at approximately 27.82°, 37.02°, 39.70°, 42.14°, 55.28°, and 57.52° are consistent with monoclinic VO_2(M), which is a rutile-like VO_2 polymorph. The peaks at 27.82° and 37.02° are mainly characteristic of VO_2(M). This suggests that a significant portion of the vanadium was reduced from V^{5+} to V^{4+} during annealing. Meantime, the peaks at 20.50°, 21.96°, 31.16°, 34.64°, 41.38°, 44.64°, 47.56°, 52.82°, and 60.00° suggest the existence of residual V_2O_5 or V_2O_5-like domains.

Table 1. XRD peak analysis of V_xO_y nanotubes after 520 °C annealing.

2θ (°)	d (Å)	β (°)	D (nm)	ε (%)	δ (×10¹⁴ m⁻²)	Phase
20.50	4.3289	0.14	57.6652	0.0601	3.0073	V_2O_5 (001)
21.96	4.0443	0.18	44.9580	0.0771	4.9475	V_2O_5 (101)
26.42	3.3708	0.22	37.0919	0.0935	7.2685	V_6O_{13}/V_2O_5 (110)
27.82	3.2043	0.20	40.9215	0.0847	5.9717	VO_2(M) (011)
31.16	2.8680	0.22	37.4878	0.0925	7.1157	V_2O_5 (400)
34.64	2.5874	0.18	46.2312	0.0750	4.6787	V_2O_5 (310)
37.02	2.4264	0.12	69.8140	0.0497	2.0517	VO_2(M) (200)
39.70	2.2685	0.16	52.7882	0.0657	3.5886	VO_2(M) (020)
41.38	2.1802	0.08	106.1497	0.0327	0.8875	V_2O_5 (002)
42.14	2.1426	0.19	44.8078	0.0774	4.9807	VO_2 (210)/V_2O_5 (312)
44.64	2.0283	0.18	47.7095	0.0727	4.3933	V_2O_5 (202)
47.56	1.9103	0.18	48.2296	0.0719	4.2991	V_2O_5 (600)
52.82	1.7318	0.18	49.2779	0.0703	4.1181	V_2O_5 (220)
55.28	1.6604	0.18	49.8205	0.0696	4.0289	VO_2 (211)/V_2O_5 (021)
57.52	1.6010	0.22	41.1917	0.0842	5.8936	VO_2 (220)
60.00	1.5406	0.20	45.8664	0.0756	4.7535	V_2O_5 (301)

The data suggest that the reduction remained incomplete under these traditionally applied conditions. The strong reflection at 26.42° is difficult to assign. It could be the V_2O_5 (110) reflection; however, in an annealed, reduced vanadium oxide it might be constructed from a Magnéli phase e.g., V_6O_{13}, V_4O_9, or V_3O_7. VO_2(B) cannot be excluded entirely, even though its characteristic reflections are not distinctly dominant, leaving VO_2(M) and the Magnéli phases the most likely candidates.

Crystallite sizes estimated from the main reflection peaks are mostly between 37nm and 70 nm (the weak reflection is excluded). Broadening of this kind is expected for nanocrystalline walls rather than bulk-like material. Microstrain stays low, roughly between 0.03% and 0.09%, and dislocation densities are on the order of 10^{14} m^{-2}; these values are typical of nanocrystalline oxides that inherit defects from ALD and the subsequent anneal.

The XRD measurement alone cannot resolve the phase assignment. Reflections from closely related vanadium oxides overlap heavily, particularly among the Magnéli phases and the VO_2 polymorphs. The high aspect ratio of the nanotube arrays combined with possible preferred orientation distorts relative peak intensities. The quantitative phase fractions cannot be extracted from this pattern with any confidence. The HRTEM/FFT is the more reliable test for oxidation state and phase distribution.

Taken together, the XRD results indicate that the 520 °C anneal converts the ALD-derived V_xO_y nanotubes into a nanocrystalline, mixed-valence oxide. VO_2(M)-like domains predominate, with residual V_2O_5 and probable Magnéli-type phases. The annealing at 520 °C supplies enough energy to crystallize the material and reduce it partially, however this strategy is not enough to reach phase-pure VO_2 or a fully reduced vanadium oxide.

Downloaded from https://nanomatimp.uomustansiriyah.edu.iq/

Copyright © 2026. This work licensed under a Creative Commons Attribution Noncommercial 4.0 International License.

Figure 4a shows the morphology of the V_xO_y nanotubes deposition. A hollow nanotube with a well-defined and continuous wall. The wall appears dense yet no clear parallel lattice fringes are presented.

The FFT in **Figure 4b** consists of a bright central spot and diffuse rings (marked in yellow). The spots are broad and markedly less sharp than those of the highly crystalline, and the rings point to many small crystallites in random orientation. **Figure 4c** shows the inverse FFT of the masked regions reconstructed in real space. The resulting fringes appear but are discontinuous and wavy, breaking into small, localized domains. Coherence therefore extends only over short distances, in line with the broadened XRD peaks and the crystallite sizes estimated from them.

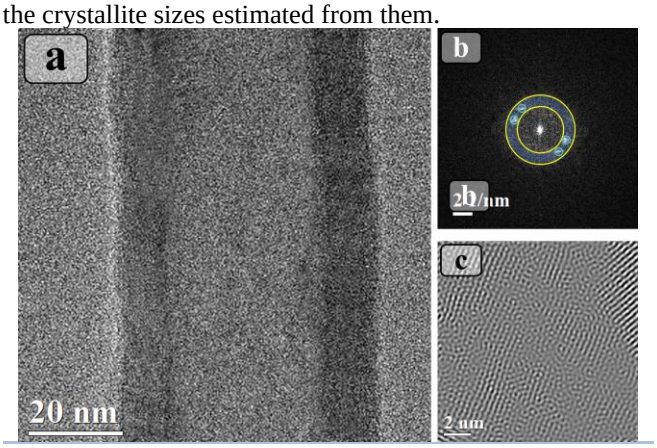


Figure 4. (a) TEM image of a VxOy nanotube annealed at 400 °C. (b) Corresponding FFT of the selected area. (c) Inverse FFT of the applied masks in (b).

Crystallinity of ALD Growth

The XRD pattern of the highly crystalline growth (two-step deposited) VO_2 nanotube arrays after the 520 °C for 2 h anneal of the 60-cycle seed-mediated oriented layer, followed by 340 additional ALD cycles at 400 °C, is shown in **Figure 5**. In contrast to the previous one-step annealed sample, this pattern is dominated by sharp, high-intensity reflections that match monoclinic VO_2(M) (rutile-like VO_2, JCPDS 43-1051). No significant V_2O_5 reflections are observed, indicating that the controlled two-step deposition successfully suppressed oxidation to V^{5+} and that the two-step strategy produced a highly crystalline, phase-pure VO_2(M) nanotube array.

The strongest reflection appears at 2θ = 27.80°, with a maximum intensity. Other prominent peaks demonstrated in **Table 2**. The XRD results confirm that the two-step deposition strategy was highly effective. The initial 60-cycle ALD layer (~2.4 nm) served as a continuous seed-mediated layer covering the entire AAT surface. Annealing this seed-mediated layer at 520 °C for 2 h under a controlled Ar atmosphere crystallized it into VO_2 without oxidizing it to V_2O_5. The subsequent 340 ALD cycles at 400 °C then grew a crystalline VO_2 layer on the seed-mediated, resulting in a total wall thickness of ~16 nm and a total of 400 cycles.

The XRD pattern is dominated by VO_2(M) and shows sharp, intense peaks. The main peak at 27.80° is roughly three times more intense than the strongest peak in the one-step annealed sample, and the pattern is cleaner overall, with no obvious V_2O_5 peaks. Crystallinity and phase purity are therefore improved.

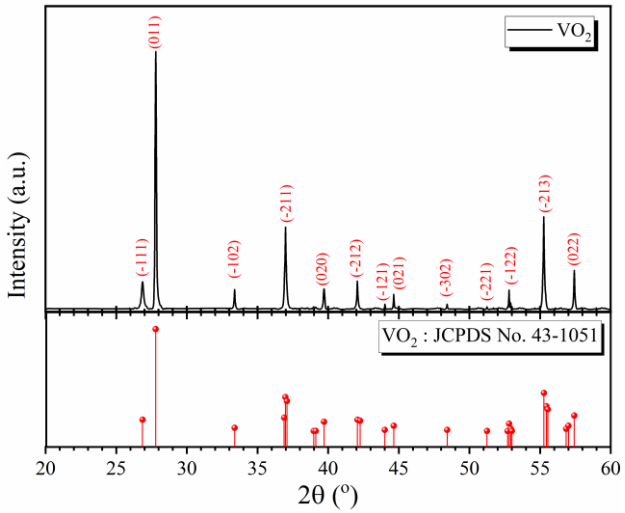


Figure 5. XRD Pattern of two-step highly crystalline growth of VO_2 nanotube.

Table 2. XRD peak analysis of two-step VO_2 nanotube arrays.

2θ (°)	d (Å)	β (°)	D (nm)	ε (%)	δ (10^{14} m^{-2})	Phase
26.84	3.3190	0.221	36.9561	5.3741	7.3220	(-111)
27.80	3.2065	0.217	37.7140	5.2661	7.0306	(011)
33.38	2.6822	0.271	30.6040	6.4896	10.6769	(-102)
36.98	2.4289	0.198	42.3066	4.6945	5.5871	(-211)
39.70	2.2685	0.212	39.8402	4.9851	6.3002	(020)
42.06	2.1465	0.276	30.8377	6.4404	10.5157	(-212)
44.64	2.0283	0.253	33.9435	5.8511	8.6793	(021)
48.42	1.8784	0.257	33.8925	5.8599	8.7055	(-302)
51.24	1.7815	0.248	35.5263	5.5904	7.9232	(-221)
52.80	1.7324	0.252	35.1954	5.6430	8.0729	(-112)
55.26	1.6610	0.296	30.2935	6.5561	10.8969	(-213)
57.42	3.3190	0.275	36.9561	5.3741	7.3220	(022)

The apparent crystallite sizes are large, 30-42 nm, and microstrain averages is around 4-6%. Dislocation densities are within 10^{14} m^{-2} rang, below those of the previous mixed-phase sample, which is consistent with better crystallinity. Those apparent sizes nevertheless exceed the ~16 nm wall thickness is due to either the Scherrer equation overestimates the coherent domain size when instrumental broadening is left uncorrected, or the VO_2 layer may be continuous and well-ordered along the nanotube, accordingly coherence extends over long distances in certain crystallographic directions. The reported and calculated data in **Table 2** are therefore apparent sizes, not physical grain sizes.

The XRD data also show that the two-step route delivers the intended phase. A seed-mediated layer was crystallized under Ar gas flow at 520 °C, followed by ALD growth at 400 °C, and the product is highly crystalline, phase-pure VO_2(M). The Ar anneal suppresses oxidation to V_2O5, and the oriented seed layer appears to template the crystallinity of the VO_2 grown on top. This is a clear gain over the one-step annealed

Downloaded from https://nanomatimp.uomustansiriyah.edu.iq/

Copyright © 2026. This work licensed under a Creative Commons Attribution Noncommercial 4.0 International License.

route, which gave mixed-valence V_xO_y with residual V_2O_5 and Magnéli phases.

HRTEM provided a local check on structure and phase purity (**Figure 6**). In **Figure 6a**, lattice fringes run continuously across the nanotube wall, with no substantial amorphous regions or structural defects in view. The region marked by the rectangle, magnified in **Figure 6b**, resolves a periodic atomic arrangement, consistent with a dense, well-ordered product of the two-step strategy.

The FFT in **Figure 6c** shows sharp diffraction spots, indicating a highly crystalline nanotube wall. The spots index to monoclinic VO_2(M) on the (-211), (011), (-102), and (-111) planes. Therefore, assignment comes from a local probe rather than bulk diffraction, it corroborates the XRD result and earlier state that declaring the annealing of the seed-mediated layer at 520 °C, followed by growth of the VO_2 layer, stabilized VO_2(M) without detectable V_2O_5 or Magnéli impurities.

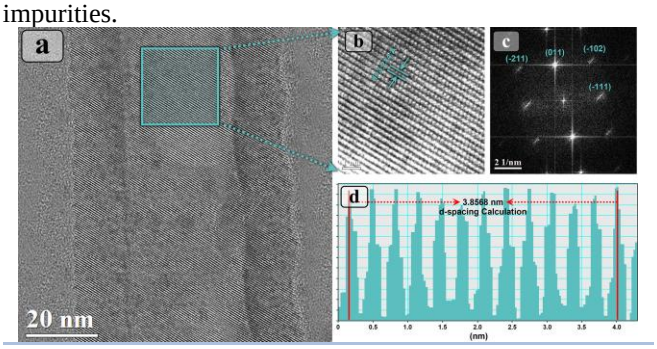


Figure 6. HRTEM analysis of a highly crystalline VO_2 nanotube. (a) TEM image of the nanotube, showing continuous parallel lattice fringes. (b) Magnified HRTEM image of the selected region, resolving the atomic lattice. (c) Corresponding FFT pattern indexed to monoclinic VO_2(M).

The magnified image and the intensity profile in **Figure 6d** give the interplanar spacing directly. The fringes are uniformly spaced at about 0.3214 nm, and the profile spans 3.8568 nm across several planes, matching the VO_2(M) spacing identified in the FFT. Therefore, periodicity persists over the full span, domains within the wall share a common crystallographic orientation, indicates higher degree of structural order.

The HRTEM results therefore show that the two-step ALD achieves highly crystalline, phase-pure VO_2(M) nanotubes with uniformly ordered walls. The initial 60-cycle seed-mediated oriented layer, crystallized under controlled Ar gas flow at 520 °C, provided an ideal template for the subsequent 340 cycle highly crystalline growth at 400 °C, resulting in a continuous and well-ordered atomic lattice. Combined with the previous XRD, SEM, and TEM dimensional analyses, these HRTEM results confirm the successful fabrication of high-quality VO_2 nanotube arrays with precise control over phase, morphology, and crystallinity.

To complement the XRD and TEM analysis with obtaining phase-selective evidence for the presence or absence of V_2O_5, Raman spectroscopy was performed on both the one-step annealed V_xO_y nanotubes and the two-step VO_2(M) nanotubes (**Figure 7**). Raman scattering is particularly sensitive to the terminal V=O stretching vibration of V_2O_5 near 994 cm^{-1}, a mode that does not overlap with the strongest VO_2(M) features and therefore provides a diagnostic test for residual V^{5+} oxide that is difficult to obtain from XRD alone[30, 31].

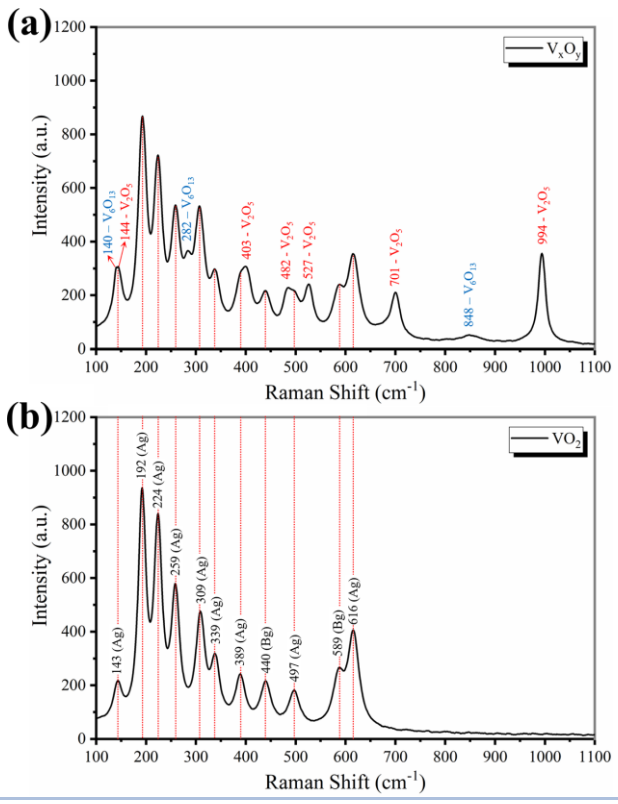


Figure 7. Raman spectra of (a) the one-step annealed V_xO_y nanotube arrays and (b) the two-step VO_2(M) nanotube arrays.

The Raman spectra were baseline-corrected and normalized for comparison. Peak positions were determined from Lorentzian/Gaussian fits to the observed bands. The VO_2(M) and V_2O_5 assignments were made by comparison with literature values[30-32].

The one-step annealed V_xO_y sample in **Figure 7a** shows, in addition to the VO_2(M) modes, clear V_2O_5 features: a strong terminal V=O stretching mode at ~994 cm^{-1}, together with modes near 700, 526, and 485 cm^{-1}. The 994 cm^{-1} peak is about twenty times higher intense than the background in that region, indicating a considerable residual V_2O_5 fraction. A weak feature near 848 cm^{-1} is consistent with residual higher oxides or possible Magnéli-type domains, in line with the XRD assignment. These observations support that the one-step anneal produces a mixed-valence, multi-phase V_xO_y material, whereas the two-step route produces phase-pure VO_2(M) within the detection limit of Raman and XRD.

In contrast, the two-step VO_2 sample in **Figure 7b** exhibits the characteristic Raman signature of monoclinic VO_2; modes at approximately 143, 192, 224, 259, 309, 338, 389, 440, 497, 588, 615, and 765 cm^{-1}, consistent with the Ag and Bg modes of VO_2(M) reported in the literature[30-32]. The low-frequency modes near 192 and 224 cm^{-1} are associated with V–V dimer vibrations, while the mode near 615 cm^{-1} is assigned to V–O stretching. Importantly, the diagnostic V_2O_5 modes at ~994,

Downloaded from https://nanomatimp.uomustansiriyah.edu.iq/

Copyright © 2026. This work licensed under a Creative Commons Attribution Noncommercial 4.0 International License.

~701, and ~527 cm^{-1} are absent, with the spectral intensity in these regions at the background level. This confirms that the two-step crystallization strategy suppresses oxidation to V^{5+} and yields VO_2(M) without detectable V_2O_5, in agreement with the XRD results.

Table 3 compiles the Raman bands expected for the three phases identified by XRD of the two deposition routes. For monoclinic VO_2(M1) ($P2_{1/c}$), group theory predicts 18 Raman-active modes (including 9 Ag and 9 Bg), of which the eleven most commonly resolved in highly crystalline VO_2(M) nanotubes are listed; the spectrum is dominated by the 192 and 224 cm^{-1} Ag pair associated with V–V dimer stretching, together with the higher-frequency V–O stretching modes near 586 and 616 cm^{-1}[31-33].

Table 3. Raman band positions and assignments in the two ALD nanotube samples.

Band (cm^{-1})	Symmetry	Assignment	Present in Figure 7
VO_2(M1) - monoclinic, $P2_{1/c}$ [31-34]			
143	A_g	V–V dimer / acoustic branch	(a) and (b)
192	A_g	V–V dimer stretching	(a) and (b)
224	A_g	V–V stretching + V–O–V bending	(a) and (b)
259	A_g	V–O–V bending	(a) and (b)
309	A_g	V–O–V bending	(a) and (b)
339	A_g	V–O–V bending	(a) and (b)
389	A_g	V–O–V bending	(a) and (b)
440	B_g	V–O–V bending	(a) and (b)
497	A_g	V–O stretching	(a) and (b)
586	B_g	V–O stretching	(a) and (b)
616	A_g	V–O stretching	(a) and (b)
V_2O_5 - orthorhombic, Pmmn [35]			
144	A_g	lattice / V–O–V	(a)
403	A_g	V–O–V bridging stretch	(a)
482	A_g	V–O–V bridging stretch	(a)
527	A_g	V–O–V bridging stretch	(a)
701	A_g	doubly coordinated oxygen stretch	(a)
994	A_g	terminal V=O stretch (diagnostic)	(a)
V_6O_{13} / Magnéli - monoclinic, C2/m (tentative; bands broad and poorly resolved) [31]			
140	—	Magnéli V–O framework	(a)
282	—	Magnéli V–O framework	(a)
848	—	Magnéli V–O framework	(a)

Orthorhombic V_2O_5 (Pmmn) is distinguished by the terminal V=O stretching mode at 994 cm^{-1}, the strongest line in its spectrum, which falls in a region where VO_2(M1) is essentially silent; the bridging V–O–V bands at 403, 482, 527 and 701 cm^{-1} provide secondary confirmation[35]. The 950–1050 cm^{-1} window therefore constitutes the decisive test for residual V^{5+} its presence indicates incompletely reduced vanadium oxide, whereas its absence is consistent with phase-pure VO_2(M). Magnéli phases, which are the expected minority products under mildly reducing conditions, give broad and poorly resolved bands that raise the background between 600 and 1000 cm^{-1} rather than producing sharp lines[31], and are consequently difficult to identify from a single spectrum. Applied to the present samples, this framework predicts that the two-step sample should exhibit only the VO_2(M1) modes, while the one-step annealed sample should additionally show the 994 cm^{-1} V_2O_5 line, consistent with the additional reflections observed at 20.50°, 34.64°, and 47.56°, in its diffractogram (**Figure 3**). Because the nanotube arrays are textured along the pore axis, the relative intensities in **Table 3** are qualitative and may differ from those of an unoriented powder.

Taken together, the XRD, HRTEM, and Raman data provide complementary evidence; XRD and HRTEM establishe the long-range crystalline VO_2(M) lattice and reveals the absence of V_2O_5 reflections, while Raman provides a phase-selective probe of the V^{5+}-O terminal bond that is insensitive to overlap with VO_2(M) reflections. All results point to the same assumption that controlled crystallization of the seed-mediated oriented layer under Ar is essential for preventing V^{5+} accumulation and for stabilizing phase-pure VO_2(M) in the nanotube arrays.

Conclusion

Highly crystalline, phase-pure monoclinic VO_2(M) nanotube arrays were fabricated by a two-step atomic layer deposition strategy inside anodic alumina templates. The 60-cycle ALD seed-mediated oriented layer, annealed at 520 °C for 2 h under controlled Ar, crystallized into VO_2 without oxidizing to V_2O_5. Subsequent 340 ALD cycles at 400 °C grew a crystalline VO_2 layer on the seed-mediated oriented, producing a total wall thickness of ~16 nm and a nanotube diameter of 60 nm. XRD of the one-step annealed sample showed a mixed-phase V_xO_y material dominated by VO_2(M), with residual V_2O_5 and Magnéli phases. In contrast, the two-step sample gave only sharp, high-intensity VO_2(M) reflections. HRTEM and FFT showed continuous lattice fringes and sharp spots indexed to VO_2(M), with a measured d-spacing of about 3.214 Å, and Raman spectroscopy found no V_2O_5 band at 994 cm^{-1} in the two-step nanotubes. The Ar anneal of the seed layer was the preventer of oxidation and allowed the subsequent crystalline growth, while the AAT set the tube diameter and wall thickness. Against conventional one-step deposition, this route gives phase-pure VO_2 nanotubes with high crystallinity and uniform morphology, which is useful for smart windows, sensors, and energy storage, where the metal–insulator transition does the functional work.

Acknowledgment

The author thanks the RES Laboratory at the College of Sciences, Mustansiriyah University, Baghdad, Iraq, for support.

Statement on Data Availability

All included data are available in this publication, form details contact the author.

Declaration of Competing Interests

The author declares that there are no conflicts of interest regarding this article.

Funding

The authors declare that no external funding was received for this study.

Downloaded from https://nanomatimp.uomustansiriyah.edu.iq/

Copyright © 2026. This work licensed under a Creative Commons Attribution Noncommercial 4.0 International License.

References

[1] V. Devthade and S. Lee, "Synthesis of vanadium dioxide thin films and nanostructures," *Journal of Applied Physics*, vol. 128, no. 23, p. 231101, 2020. https://doi.org/10.1063/5.0027690.

[2] C. Wen *et al.*, "A review of the preparation, properties and applications of VO2 thin films with the reversible phase transition," (in English), *Frontiers in Materials*, Review vol. Volume 11 - 2024, 2024. https://doi.org/10.3389/fmats.2024.1341518.

[3] H. Ya *et al.*, "Research Progress on Mechanisms, Regulation Strategies, and Applications of Phase Transition Hysteresis of Vanadium Dioxide," *Advanced Materials*, vol. 38, no. 19, p. e16579, 2026. https://doi.org/10.1002/adma.202516579.

[4] M. Taha *et al.*, "Insulator–metal transition in substrate-independent VO2 thin film for phase-change devices," *Scientific Reports*, vol. 7, no. 1, p. 17899, 2017. https://doi.org/10.1038/s41598-017-17937-3.

[5] F. Dumas-Bouchiat, M. Gaudin, I. A. Alonzo Zapata, and C. Champeaux, "VO2 thin films: various microstructures for hysteresis manipulations," *Vacuum*, vol. 227, p. 113408, 2024. https://doi.org/10.1016/j.vacuum.2024.113408.

[6] A. Nikolenko *et al.*, "Controllable tuning of reversible thermally induced phase transition and adaptive infrared emissivity in microcrystalline VO2 thin films via argon ion implantation," *Thin Solid Films*, vol. 830, p. 140810, 2025. https://doi.org/10.1016/j.tsf.2025.140810.

[7] Z. Baji *et al.*, "VO2 layers with high resistive switching ratio by atomic layer deposition," *Materials Science in Semiconductor Processing*, vol. 162, p. 107483, 2023. https://doi.org/10.1016/j.mssp.2023.107483.

[8] I. Ahmed *et al.*, "Thickness-dependent structural evolution of VO2 (M1) thin films and photodetection in n-VO2/p-Si heterojunctions," *Journal of Materials Science: Materials in Electronics*, vol. 37, no. 22, p. 1740, 2026. https://doi.org/10.1007/s10854-026-18135-6.

[9] Z. Khan, P. Singh, S. A. Ansari, S. R. Manippady, A. Jaiswal, and M. Saxena, "VO2 Nanostructures for Batteries and Supercapacitors: A Review," *Small*, vol. 17, no. 4, p. 2006651, 2021. https://doi.org/10.1002/smll.202006651.

[10] A. Firdous and A. Ashraf, "Critical Review on the Phase Change Properties of VO_2: Influence of Synthesis Methods and Transition Mechanisms," *Journal of Engineering, Science and Technological Trends*, vol. 2, no. 2, 2025. https://doi.org/10.64060/jestt.v2i2.2.

[11] Y. Wang, X. Wang, J. Zhang, Q. Lin, and H. Xu, "Phase-Change VO2 Enabled Optoelectronic Devices With Switching Dynamics," *Advanced Optical Materials*, vol. 13, no. 36, p. e02649, 2025. https://doi.org/10.1002/adom.202502649.

[12] J. H. Lee, J. Y. Kim, H.-J. Lee, S.-J. Choi, Y. J. Lee, and H. W. Jang, "Beyond the Silicon Plateau: A Convergence of Novel Materials for Transistor Evolution," *Nano-Micro Letters*, vol. 18, no. 1, p. 69, 2025. https://doi.org/10.1007/s40820-025-01898-8.

[13] Z. Zheng *et al.*, "Remote Epitaxy and Phase Diagram of Single-Crystalline Ultrathin VO2 Films on the TiO2(001) Substrate," *ACS Applied Materials & Interfaces*, vol. 17, no. 51, p. 70203–70216, 2025. https://doi.org/10.1021/acsami.5c18705.

[14] E. Kessels, A. Devi, J.-S. Park, M. Ritala, A. Yanguas-Gil, and C. Wiemer, "Atomic layer deposition," *Nature Reviews Methods Primers*, vol. 5, no. 1, p. 66, 2025. https://doi.org/10.1038/s43586-025-00435-6.

[15] J. Cyriac *et al.*, "A Pervasive Study on the Fabrication Techniques of Nanotechnology," in *A Journey from Nanotechnology to Picotechnology: Atomic and Molecular Scale Engineering*, S. Kulkarni, Ed. Cham: Springer Nature Switzerland, 2026, pp. 45–90. https://doi.org/10.1007/978-3-032-07228-3_3.

[16] V. T. Lukong, K. Ukoba, and T.-C. Jen, "Fabrication of vanadium dioxide thin films and application of its thermochromic and photochromic nature in self-cleaning: A review," *Energy & Environment*, vol. 34, no. 8, p. 3495–3528, 2023. https://doi.org/10.1177/0958305X221145204.

[17] B. V. Voloshin, V. A. Seleznev, and V. A. Golyashov, "Atomic Layer Deposition Synthesis of thin Films of Vanadium Oxides in a Reducing Hydrogen Atmosphere," *Journal of Structural Chemistry*, vol. 65, no. 10, p. 2073–2087, 2024. https://doi.org/10.1134/S0022476624100160.

[18] S. Chackrabarti and R. A. Zargar, "Review: vanadium pentoxide thin films-advanced doping strategies and interface engineering for next-generation applications," *Journal of Materials Science*, vol. 61, no. 8, p. 4894–4938, 2026. https://doi.org/10.1007/s10853-026-12152-w.

[19] C.-Y. Kim, S. H. Kim, S. J. Kim, and K.-S. An, "VO2(110) film formation on TiO2(110) through post-reduction of ALD grown vanadium oxide," *Applied Surface Science*, vol. 313, p. 368–371, 2014. https://doi.org/10.1016/j.apsusc.2014.05.216.

[20] A. Al-Haddad, Z. Zhan, C. Wang, S. Tarish, R. Vellacheria, and Y. Lei, "Facile Transferring of Wafer-Scale Ultrathin Alumina Membranes onto Substrates for Nanostructure Patterning," *ACS Nano*, vol. 9, no. 8, p. 8584–8591, 2015. https://doi.org/10.1021/acsnano.5b03789.

[21] A. Al‐Haddad, Z. Wang, M. Zhou, S. Tarish, R. Vellacheri, and Y. Lei, "Constructing Well‐Ordered CdTe/TiO_2 Core/Shell Nanowire Arrays for Solar

Downloaded from https://nanomatimp.uomustansiriyah.edu.iq/

Copyright © 2026. This work licensed under a Creative Commons Attribution Noncommercial 4.0 International License.

Energy Conversion," *Small*, vol. 12, no. 40, p. 5538–5542, 2016.

https://doi.org/10.1002/smll.201601412.

[22] A. Al-Haddad *et al.*, "TiN@Al_2O_3/Al nanocapacitor based on anodic aluminum oxide template," in *AIP Conference Proceedings*, 2020, vol. 2307, no. 1: AIP Publishing.

https://doi.org/10.1063/5.0033137.

[23] R. M. Hameed, A. Al-Haddad, and A. K. Albarazanchi, "Facile transformation of graphene oxide nanospheres based on AAO template," *Kuwait Journal of Science*, vol. 50, no. 4, p. 563–568, 2023.

https://doi.org/10.1016/j.kjs.2023.08.002.

[24] A. Al-Haddad *et al.*, "Dimensional Dependence of the Optical Absorption Band Edge of TiO_2 Nanotube Arrays beyond the Quantum Effect," *The Journal of Physical Chemistry C*, vol. 119, no. 28, p. 16331–16337, 2015.

https://doi.org/10.1021/acs.jpcc.5b02665.

[25] H. A. Al-Zuhairy, A. Al-Haddad, and A. M. Abbas, "NiO Nanowire Arrays Based on AAO Templates for Photoelectrochemical Water Splitting " *Iraqi Journal of Environmental Sciences*, vol. 2, no. 2, p. 45–59, 2026.

https://doi.org/10.23851/ijes.v2i2.41.

[26] Y.-C. Lin *et al.*, "Advancing Nanopore Technology: Anodic Aluminum Oxide Membranes with Anisotropic Pores through Controlled Stretching for Applications in Nanopatterning," *ACS Applied Nano Materials*, vol. 7, no. 12, p. 14707–14718, 2024.

https://doi.org/10.1021/acsanm.4c02257.

[27] C.-A. Ku and C.-K. Chung, "Advances in Through-Hole Anodic Aluminum Oxide (AAO) Membrane and Its Applications: A Review," *Nanomaterials*, vol. 15, no. 21, p. 1665, 2025.

https://doi.org/10.3390/nano15211665.

[28] M. Yass, M. J. M. Ali, A. Al-Haddad, A. Jaafar, L. Himics, and M. Veres, "Utilizing ZnO nanoparticles to improve the optical absorption of a green synthesized bioorganic polymer," *AIP Conference Proceedings*, vol. 3211, no. 1, p. 070003, 2025.

https://doi.org/10.1063/5.0257065.

[29] A. Y. Al-Jumaily, S. S. Al-Jubori, and A. Al-Haddad, "Green synthesized TiO_2 nanoparticles impact on extensive-drug resistance gram-negative bacteria," in *AIP Conference Proceedings*, 2024, vol. 3097, no. 1: AIP Publishing.

https://doi.org/10.1063/5.0209550.

[30] P. Schilbe, "Raman scattering in VO2," *Physica B: Condensed Matter*, vol. 316-317, p. 600–602, 2002.

https://doi.org/10.1016/S0921-4526(02)00584-7.

[31] V. M. Dzhagan *et al.*, "Raman fingerprints of different vanadium oxides as impurity phases in VO2 films," *Optical Materials*, vol. 148, p. 114894, 2024.

https://doi.org/10.1016/j.optmat.2024.114894.

[32] O. F. Kolomys, V. V. Strelchuk, P. M. Lytvyn, D. M. Maziar, V. M. Dzhagan, and O. V. Dubikovskyi, "Raman and scanning spreading resistance mapping of the evolution of structural phases near the insulator–metal transition in VO2 films," *Applied Surface Science*, vol. 715, p. 164627, 2026.

https://doi.org/10.1016/j.apsusc.2025.164627.

[33] V. V. Strelchuk *et al.*, "Effect of structural disorder on the modification of V–V and V–O bond lengths at the metal-dielectric phase transition in VO2 thin films," *Materials Science in Semiconductor Processing*, vol. 174, p. 108224, 2024.

https://doi.org/10.1016/j.mssp.2024.108224.

[34] V. Mussi *et al.*, "Polarized Raman mapping and phase-transition by CW excitation for fast purely optical characterization of VO2 thin films," *Scientific Reports*, vol. 14, no. 1, p. 19338, 2024.

https://doi.org/10.1038/s41598-024-70301-0.

[35] S. V S *et al.*, "Mechanistic insights into the formation of phase pure V2O5 2D nanostructures: Advanced fourier transform-raman spectroscopy analysis," *Thin Solid Films*, vol. 815, p. 140642, 2025.

https://doi.org/10.1016/j.tsf.2025.140642.

Downloaded from https://nanomatimp.uomustansiriyah.edu.iq/

Copyright © 2026. This work licensed under a Creative Commons Attribution Noncommercial 4.0 International License.